Soft Matter

ROYAL SOCIETY OF CHEMISTRY

PAPER

View Article Online
View Journal

Check for updates

Cite this: DOI: 10.1039/d4sm00931b

Towards a universal model for the foaming behavior of surfactants: a case study on per- and polyfluoroalkyl substances (PFAS)†

Muchu Zhou and Reza Foudazi *

Published on 23 October 2024. Downloaded on 11/23/2024 3:26:02 AM.

Received 1st August 2024,
Accepted 22nd October 2024

DOI: 10.1039/d4sm00931b

rsc.li/soft-matter-journal

Foam fractionation offers a promising solution for the separation of surface-active contaminants from water. Therefore, this work aims to comprehensively investigate foaming behavior and its correlations with the interfacial properties. As a case study, we evaluate foaming of per- and polyfluoroalkyl substances (PFAS), which are one of significant environmental issues worldwide due their pervasive presence in the environment. Since there is no universal model to describe the foaming behavior of surfactants that can be applied to PFAS, this research utilizes dimensional analysis to establish a correlation between the foaming behavior of PFAS solutions—characterized by expansion rate of foaming—and dimensionless numbers that represent both processing and interfacial characteristics. Foaming parameters, such as gas flow rate and aeration time, are varied to study their effect on PFAS foamability. In addition, we study PFAS with different headgroups and with different chain lengths in the presence of electrolytes with different concentrations. Our study elucidates distinct, condition-specific equations for individual PFAS, revealing that long-chain PFAS foaming is significantly influenced by interfacial property-related dimensionless numbers, such as the Boussinesq number. Additionally, the Froude number and Weber number affect the foamability of both long- and short-chain PFAS. Moreover, our study identifies specific trends, including a maximum foaming capacity at a certain Capillary number, aligning with the maximum in dilatational interfacial modulus. The results suggest more studies are needed on bubble interaction and foam film behavior.

1. Introduction

Partially or fully fluorinated synthetic compounds, known as per- and polyfluoroalkyl substances (PFAS), have gained broad usage in numerous industries, such as non-stick coatings, aqueous film forming foams (AFFFs), cleaners, cosmetics, and semiconductors.[1] This widespread adoption is attributed to their remarkable chemical and thermal stability, as well as their ability to repel both water and oil.[2–6] However, the extensive utilization of PFAS, coupled with their notable stability attributed to the C–F bond, has resulted in their ubiquitous presence, emerging as a global environmental concern. In addition, there are significant concerns about the toxicity and bioaccumulation of PFAS.[5,7–9] Exposure to PFAS is linked to an increased risk of obesity, reproductive dysfunction, elevated cholesterol, liver and kidney diseases, lipid and insulin dysregulation, and cancer.[10–13]

One of the pathways for human exposure to PFAS is through PFAS-contaminated water sources, with a particular emphasis on drinking water.[14–16] For example, the concentration ranges of perfluorooctanesulfonic acid (PFOS) and perfluorooctanoic acid (PFOA) in the United States (U.S.) drinking water are 0.04–1.80 ppt and 0.02–0.35 ppt, respectively.[17] Perfluorobutanesulfonic acid (PFBS) has been found with a lower detection frequency of 0.05%, but with the mean concentrations of 212 and 136 ppt in surface water and ground water, respectively.[16] In ground water, the concentration of perfluorohexanesulfonic acid (PFHxS) has been reported in 409 ppt to 1600 ppt range.[16] The U.S. Environmental Protection Agency (EPA) has issued a Maximum Contaminant Levels (MCLs) and a Maximum Contaminant Level Goals (MCLGs) for PFOS and PFOA in drinking water at 4 and 0 ng L^{-1}, respectively.[18] Moreover, MCLs have been defined for other PFAS, *e.g.*, 10 ng L^{-1} for PFHxS, perfluorononanoic acid (PFNA), and hexafluoropropylene oxide (HFPO) dimer acid and its ammonium salt (GenX).[18] These substances have been employed as alternatives to long-chain PFAS.

In addition to water sources, discharge from industrial facilities, such as semiconductor manufacturing, represents a significant contributor to PFAS emissions.[6] The concentration of PFAS in industrial wastewaters is typically several orders of magnitude higher than that in domestic waters, for instance, reaching a total PFAS concentration of 40 000 ng L^{-1} in

---

School of Sustainable Chemical, Biological and Materials Engineering, The University of Oklahoma, Norman, OK 73019, USA. E-mail: rfoudazi@ou.edu

† Electronic supplementary information (ESI) available. See DOI: **https://doi.org/10.1039/d4sm00931b**

Published on 23 October 2024. Downloaded on 11/23/2024 3:26:02 AM.

industrial wastewater.[19–21] Despite this, there is a scarcity of studies investigating the discharge of PFAS from industrial wastewater treatment plants (WWTPs) to assess their presence and overall discharge loads.[20] Moreover, industrial WWTPs often exhibit limited efficacy in PFAS removal, with the transformation of PFAS precursors into perfluoroalkyl acids (PFAA) occurring during biological treatment processes.[20] It has been suggested to implement a pretreatment on industrial wastewaters to eliminate PFAS before their release into sewer systems or the environment.[6] The common PFAS treatment technologies involve adsorption using activated carbon, high pressure membrane filtration, *in situ* degradation (oxidation), anion exchange resins, and foam fractionation.[16,22,23] Nevertheless, these PFAS remediation methods have some challenges. For instance, the membrane filtration methods, such as reverse osmosis (RO), are associated with high costs and membrane fouling, the anion exchange resins are hard to reuse, the oxidation has a low PFAS degradation efficiency, and secondary PFAS waste is generated when using adsorbents, such as activated carbon.[16,24,25]

Foam fractionation, also known as aeration or foam flotation, has been determined as a promising remediation method to remove PFAS from contaminated water due to their surfactancy nature, enabling them to adsorb at the air–water interface during foaming.[22,23,25–28] Prior to utilization for PFAS removal, foam flotation has been used in other fields, such as enhanced oil recovery (EOR),[29,30] and critical materials separation.[31–33] Several groups have used custom-made aeration collection devices to achieve PFAS removal.[34–36] Burns *et al.*[37,38] successfully integrated a surface-active foam fractionation system into WWTPs for treating 90–110 $\mathrm{m^3\ day^{-1}}$ of groundwater, aiming to remove PFAS. The removal efficiency was reported to decrease with reducing air flow rates (Q_{air}) and foaming times (t_{f}). According to Meng *et al.*,[34] the lower initial PFAS concentration (0.093 mM *vs.* 0.382 mM) results in greater fractional PFAS recovery. In addition, PFAS molecules with sulfonic acid headgroups (perfluorosulfonic acid), called PFSA, are easier to be removed compared to the ones with carboxylic acid headgroups (perfluorocarboxylic acid), known as PFCA.[35,36] It is worth noting that aeration mostly faces challenges in efficiently removing short-chain PFAS, exemplified by a removal efficiency of around 10–30% for PFBS, and no removal for perfluorobutanoic acid (PFBA).[34,35,37] Lee *et al.*[39] explored the impact of metallic activators, such as $\mathrm{Ca^{2+}}$ and $\mathrm{Fe^{3+}}$, on the PFOS and PFOA removal efficiency by using a foam flotation reactor. The introduction of $\mathrm{Fe^{3+}}$ resulted in the highest PFOS removal efficiency, reaching 99.5%. Wang *et al.*[36] also demonstrated that the valence of ions plays an important role on PFAS removal efficiency.

Another emerging challenge in PFAS cleanup is the lack of fast and low-cost detection methods. Liquid chromatography-mass spectrometry, known as LC-MS, is commonly used for PFAS detection.[23] However, LC-MS is expansive and specialized. Except for LC-MS, electroanalytical approaches, such as interfacial electrochemical process and porous polymer sensors with a molecularly imprinted polymers electrode, were reviewed by Lamichhane *et al.*[40] with a possibility to detect PFAS. In addition, Mahpishanian *et al.*[41] developed a liquid phase extraction method, where a colored methylene blue-PFAS complex is formed, to detect PFAS *via* spectrophotometric analysis.

Dimensional analysis is a powerful tool in various fields of science and engineering, including the study of foaming process. Beyond the studies focused directly on foaming,[34–39,42–51] dimensional analysis can be applied to investigate and understand foaming process more comprehensively. For instance, optimization of foaming process, scale-up and scale-down studies, comparative studies, model validation, and parameter sensitivity analysis. Nevertheless, only a few studies have focused on the dimensional analysis of foaming process based on interfacial and colloidal parameters. Bois *et al.*[52] applied dimensional analysis to surfactant solutions (sodium laureth sulfate, Tween 20, and Brij L23) to study the influence of processing parameters on their foamability. Expansion rate of foaming, $\frac{H_{\mathrm{f}}}{H_{\mathrm{l}}}$ (where H_{f} is the foam height and H_{l} is the liquid height) was used to characterize the foaming behavior of surfactant solutions, and it was found that the dimensionless numbers of Reynolds number (Re) and mixing time number control the foaming process occurring in a mechanically agitated vessel. However, the effect of interfacial properties was not taken into account. Noting that the key variables that influence the foaming behavior are the interfacial properties, such as surface tension (γ) and dilatational interfacial modulus (E).[24,42–44,48–51] For instance, Gibbs stability $\left(E > \frac{\gamma}{2}\right)$ was introduced as the criteria for determining the stability of interface stabilized by particles, and thus, the foam stability.[44–47] Mary *et al.*[53] also used dimensional analysis to predict the bubble size of the surfactant solutions, and they demonstrated that the bubble size of foams is mainly controlled but not limited by Capillary number (Ca). They also suggested that the impact of more parameters, such as interfacial rheology and kinetic diffusion of surfactants to the interfaces, needs to be investigated.

This work aims to comprehensively investigate the foaming behavior (foamability) and its correlations with the interfacial properties. Therefore, we study PFAS with different headgroups and with different chain lengths in the presence of electrolytes with different concentrations as a case study. However, the study is not limited to PFAS and can be applied to other surfactants. The foaming behavior characterized by $\frac{H_{\mathrm{f}}}{H_{\mathrm{l}}}$ is systematically analyzed by carrying out the dimensionless analysis of a lab-scale foaming column. This theoretical methodology is reinforced by conducting experiments, where processing parameters are altered, and the progression of H_{f} with t_{f} is observed. Considering that interfacial parameters of PFAS are measured and reported in our recent work,[24] the objective of this study is to enhance our comprehension of the primary physical phenomena that predominantly influence foam formation in the aeration process.

2. Experimental and methods

2.1. Materials

KPFOS (heptadecafluorooctanesulfonic acid potassium salt, ≥98.0%, CAS: 2795-39-3), PFOA (perfluorooctanoic acid, 95%, CAS: 335-67-1), and KPFBS (potassium nonafluoro-1-butanesulfonate, 98%,

Published on 23 October 2024. Downloaded on 11/23/2024 3:26:02 AM.

CAS: 29420-49-3) were purchased from Sigma-Aldrich. The chemical structure of PFAS compounds used in this work is shown in Fig. 1. Sodium chloride (NaCl) and calcium chloride ($CaCl_2$) were purchased from Fisher BioReagents (≥99.0%, CAS: 7647-14-5) and Thermo Scientific (97%, CAS: 10043-52-4), respectively. All samples were prepared using deionized water produced through Millipore Synergy® Water Purification System and no additional purification of the chemicals was conducted. Lower-concentration PFAS aqueous solutions were prepared through a dilution of higher-concentration PFAS stock solutions. Table 1 presents the composition of the PFAS aqueous solutions analyzed in this study.

2.2. Foaming behavior analysis

The dynamic foaming behavior of PFAS aqueous solutions was recorded and analyzed by using the foam analyzer (Krüss Scientific, DFA 100) with ADVANCE software. The setup is shown in Fig. S1A (ESI†). About 30 mL of PFAS aqueous solution was added into a prism column (CY4572) of 40 mm inner diameter with a max volume of 230 mL, which was fixed onto the sample holder. An O-ring was placed onto the sample holder, followed by a glass filter and another O-ring for sealing as seen in Fig. S1B (ESI†). Two glass filters with a pore size ranging of 16–40 μm (FL4503, ∅ 50 mm) and 40–100 μm (FL4502, ∅ 50 mm), respectively, were used to aerate the PFAS aqueous solution (Table 2).

The PFAS aqueous solution in the prism column was sparged with air at various Q_{air} ranging from 0.2 to 1.0 L min^{-1} for different t_f of 30, 60, 120, and 300 s to create the PFAS aqueous foams. The video showing the foaming process is available as ESI.† The Q_{air} and t_f play important roles in determining the properties of created foams. Given the Q_{air} at 0.2 L min^{-1}, 30 s is enough for KPFBS and PFOA foams to reach the steady state, while it takes about 100 s for KPFOS foams to reach the dynamic equilibrium. Two liquid content sensors were placed inside the prism column, and each of the sensors has seven chips to measure the liquid content (ε) and resistance (the inverse of the electrical conductivity) across the foam at different heights, and one chip on the bottom as the reference (Fig. S1B, ESI†). A camera (2 fps at 1280 × 1024 px), of which the vertical position can be changed, was used to record the foam structure during the foaming process through the prism attachment of the prism column as seen in Fig. S1C (ESI†). Trials for this experiment were conducted at room temperature and the pH was not adjusted. For each formulation, at least two replicates were done.

2.3. Dynamic surface tension

To determine the γ of PFAS aqueous solutions at 25 ± 0.5 °C, the Wilhelmy plate tensiometer (Dataphysics, DCAT 25) was utilized. The γ data points were recorded over a 1 h period, with a minimum of two replicates conducted for each composition. The instrument was calibrated prior to use. The platinum plate was meticulously cleaned by using a Bunsen burner before each measurement to ensure its dryness and cleanliness. The equilibrium surface tension was determined from the intercept of dynamic surface tension against $t^{-0.5}$.[24]

Table 1 Composition of PFAS aqueous solutions used in the present work

PFAS	Concentration (mM)	Salt	Concentration (mM)
KPFOS	0.01–1.11	NaCl	0.5, 1, 5, 10, 50, 100, and 200
		$CaCl_2$	0.1, 0.5, 1, 5, 10, 50, and 100
PFOA	0.40	NaCl	0.5, 1, 5, 10, 50, 100, and 200
KPFBS	0.40	$CaCl_2$	0.1 and 100

2.4. Dilatational interfacial rheology

The pendent drop tensiometer (Attension KSV Instruments, Biolin Scientific, Finland) was used to characterize the dilatational interfacial rheology of the PFAS-adsorbed air–water interface at room temperature. The pendent drop volume periodically oscillated in the linear viscoelastic range at 0.5 Hz, and the oscillation of γ and surface area (A) were recorded accordingly. The γ was determined by the software according to the Young–Laplace equation.[54] The definition of E is as follows:[24,55–57]

$$E = A_0\frac{\Delta\gamma}{\Delta A} = \frac{\mathrm{d}\gamma}{\mathrm{d}\ln A} \tag{1}$$

where A_0 represents the average surface area and an amplitude area variation (ΔA) occurs around the A_0, and $\Delta\gamma$ is the amplitude of the γ deviation from the average γ_0. E is a complex number comprising the dilatational storage modulus, E' (dilatational surface elasticity), as its real part, and the dilatational loss modulus, E'', as its imaginary part. The eqn (2a) and (2b) are used to obtain the E' and E'':[24,55,56]

$$E' = |E|\cos(\phi) \tag{2a}$$

$$E'' = |E|\sin(\phi) = 2\pi f\eta_s \tag{2b}$$

where f is the frequency, and η_s is the dilatational surface viscosity. The details were described in our previous work.[24] Each measurement was repeated three to five times to obtain the average and standard deviation.

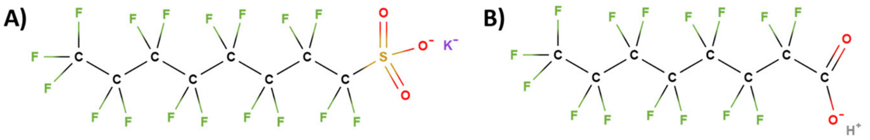

Fig. 1 Chemical structure of (A) KPFOS, (B) PFOA, and (C) KPFBS.

View Article Online

Published on 23 October 2024. Downloaded on 11/23/2024 3:26:02 AM.

Table 2 Setup of DFA 100

Glass filter pore size range (D_f, µm)	16–40 and 40–100
Sample volume (mL)	30
Q_{air} (L min^{-1})	0.2–1.0
t_f (s)	30–300
Camera position	60 mm from H_{l0} (initial liquid level)

3. Results and discussion

3.1. Foaming capacity of PFAS aqueous solutions

Two important foaming characteristics are capacity (foamability) and stability, both of which are affected by the foam preparation parameters, t_f and Q_{air}, and cross-section area of foam column. For example, Pal *et al.* prepared foams stabilized by gemini surfactants and reported that 300 s of agitation resulted in the foams with largest volume, while a smaller volume was obtained by stirring the system for 400 s due to the increased bubble rupture tendency.[30,34] In this study, we only discuss foamability and the foam stability will be presented in future works. Fig. 2A shows the H_f of 0.4 mM KPFOS aqueous foams during the 30 s of aeration by using Q_{air} of 0.2, 0.4, and 0.6 L min^{-1}, and two glass filters with D_f of 40–100 and 16–40 µm, respectively. The H_f increases with an increase in Q_{air}. It should be mentioned that the use of the filter with a smaller D_f has no significant impact on the H_f, while the kinetics of foaming, $\dot{H}_f = \frac{dH_f}{dt}$, is slightly affected. For example, lower $\dot{H}_f$ is obtained at the beginning of foaming by using the Q_{air} of 0.2 L min^{-1} and smaller D_f. Furthermore, the H_f does not approach the equilibrium status at 30 s for KPFOS. The system can be considered to reach the equilibrium once the H_f measurements show that the changes fall below a predetermined threshold, and the corresponding time is noted as the equilibrium time (t_e). The equation below is used to define the H_f change:

$$|\Delta H_f| = \frac{H_{f,t+\Delta t} - H_{f,t}}{H_{f,t+\Delta t}} \times 100\% \qquad (3)$$

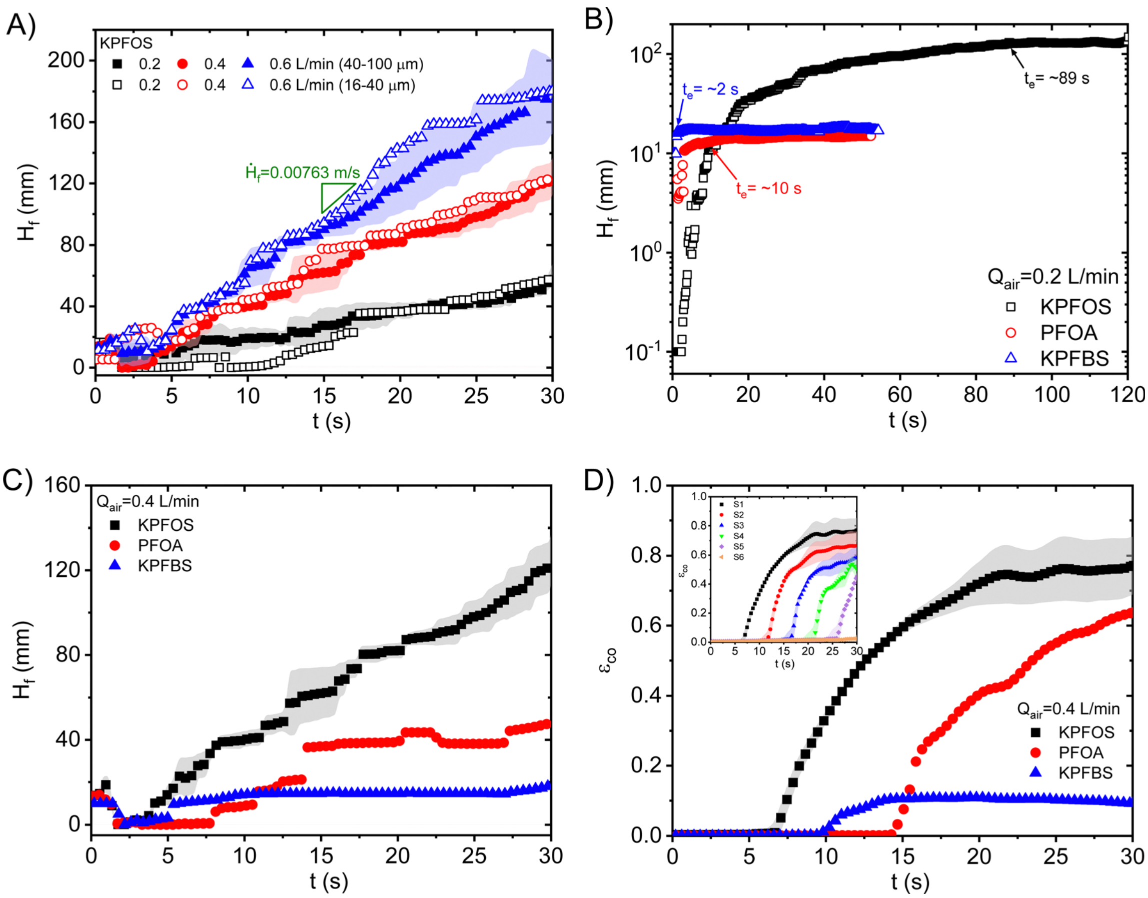

Fig. 2 (A) Foam height of 0.4 mM KPFOS aqueous foams during 30 s of aeration by using various air flow rates of 0.2, 0.4, and 0.6 L min^{-1}, and two filters with different pore size ranges of 16–40 and 40–100 µm, respectively. (B) Foam height of 0.4 mM KPFOS, PFOA, and KPFBS aqueous foams as a function of aeration time, showing the various times used to approach the equilibrium status. The air flow rate was 0.2 L min^{-1}, and the filter size was 40–100 µm. (C) Foam height of 0.4 mM KPFOS, PFOA, and KPFBS aqueous foams during 30 s of aeration, indicating that the foaming capacity has the following order: KPFOS > PFOA > KPFBS. The pore size range of filter was 40–100 µm, and the air flow rate was 0.4 L min^{-1}. (D) corrected liquid content of 0.4 mM KPFOS, PFOA, and KPFBS aqueous foams during 30 s of aeration based on the values provided by the first sensor chip. The inset is the corrected liquid content of 0.4 mM KPFOS at various heights of foam. The shaded area shows the experimental error bar.

This journal is © The Royal Society of Chemistry 2024

Published on 23 October 2024. Downloaded on 11/23/2024 3:26:02 AM.

If the $|\Delta H_f|$ is smaller than 1.5% within 10 s, then the beginning of this 10 s period is considered as the t_e. Examples of H_f equilibrium status are shown in Fig. 2B. After the equilibrium, H_f drops a little bit and undergoes a small oscillation because the foam structure is separated by some large air bubbles. According to Amani and Firouzi,[58] the flow regime in a vertical tube/pipe during the aeration includes (1) bubble, (2) foamy bubble, (3) slug flow, (4) churn flow, and (5) annular flow, depending on the Q_{air}. Our result suggests that when slowly sparging the solutions, the KPFOS foaming flow regime transits from foamy bubble to slug flow/churn flow once the H_f reaches the steady state. When the $Q_{air} >$ 0.2 L min^{-1}, the equilibrium status for KPFOS foams cannot be reached by using DFA 100 due to the overflow alarm, for instance, the H_f reached the overflow alarm height at 36 s when the Q_{air} was 0.4 L min^{-1}, yet the equilibrium status was not even approaching.

Compared to KPFOS, PFOA and KPFBS reach equilibrium status in shorter durations when the Q_{air} is 0.2 L min^{-1} (Fig. 2B). However, at 0.2 L min^{-1}, PFOA and KPFBS only have a thin layer of bubbles on the top of solutions. Fig. 2C shows the H_f of 0.4 mM KPFOS, PFOA, and KPFBS foams within the 30 s of aeration for Q_{air} of 0.4 L min^{-1}, implying that the KPFOS have the best foamability. When increasing the Q_{air} to 0.6 L min^{-1}, the KPFOS still have the best foaming capacity as seen in Fig. S2 (ESI†). Furthermore, the ε of foams is another crucial concept determining the structure of foams,[49,59] which is defined as follows:

$$\varepsilon = \frac{V_{\text{liquid}}}{V_{\text{foam}}} \tag{4}$$

where V_{liquid} is the volume of liquid in the foams with a volume of V_{foam}.[59] Bubble deformation is no longer observed as jamming transition is approached when $\varepsilon \sim 0.36$, whilst the bubbly liquid is formed if $\varepsilon > 0.36$.[49,59] On the other hand, the foams have polyhedral bubbles if $\varepsilon \leq 0.05$.[49] For 0.4 mM KPFOS foams (D_f was 40–100 μm and Q_{air} was 0.2 L min^{-1}), only the first two sensor chips have the reading for 30 s foaming, whereas all sensor chips have the reading when t_f is increased to 120 s. The ε across the foams can be correlated with the foam conductivity (σ_{foam}) and liquid conductivity (σ_{ref}, according to resistance obtained from the chip on the bottom) as follows:[44,49,60]

$$\varepsilon_{\text{co}} = \frac{3\sigma(1+11\sigma)}{1+25\sigma+10\sigma^2} \tag{5}$$

where σ is the ratio of $\sigma_{\text{foam}}/\sigma_{\text{ref}}$, called relative conductivity. Fig. 2D is the $\varepsilon_{\text{co\_1}}$ (the first sensor chip position) of 0.4 mM KPFOS, PFOA, and KPFBS aqueous foams, indicating that the KPFOS foams hold more water, whereas the KPFBS foams are relatively drier. Additionally, the $\varepsilon_{\text{co\_1}}$ of PFOA foams keeps increasing slightly beyond the time that foam height has already approached the equilibrium status. When the Q_{air} is 0.4 L min^{-1}, the foams only reach the first sensor chip for PFOA and KPFBS, but for KPFOS, six sensor chips have the readings as shown in the inset of Fig. 2D.

Fig. 3 shows the foam structure at t_f of 10, 20, and 30 s for 0.4 mM PFAS foams created by employing different conditions. During foaming, the camera captures the bubbles at 13–15 s for KPFOS foams when the Q_{air} is 0.2 L min^{-1}. Different types of bubble radius are obtained from DFA 100. Fig. S3A (ESI†) shows the average bubble radius (R_{ave}) and Sauter mean bubble radius (R_{32}) of KPFOS foams. The bubble size becomes smaller with aerating. The R_{32} keeps decreasing until reaching the steady state approximately close to equilibrium H_f. Fig. S3B (ESI†) depicts the bubble count per mm^2. Expectedly, the D_f has an impact on the bubble size of PFAS foams. Smaller bubble size is obtained by using the filters with a smaller D_f as shown in Fig. 3A and B. However, when the steady state is reached, the foams sparged by a smaller D_f have a greater R_{32} as seen in Table S1 (ESI†). The greater difference between R_{ave} and R_{32} indicates the presence of very large bubbles when using smaller D_f, leading to increased drainage and reduced foam stability. In this study, the R_{32} is used for discussion, and the last 10 data points before stopping aeration are used to obtain the final bubble radius as R. Fig. S4 (ESI†) presents another foam trial for 0.4 mM KPFOS but extending the t_f to 120 s. It is clear that the bubble size distribution becomes narrower as the KPFOS foam reaches the steady state.

For 0.4 mM PFOA and KPFBS aqueous solutions, the bubbles were not captured by the camera due to the insufficient H_f for camera field of view at 0.2 L min^{-1} flow rate. When Q_{air} is 0.4 L min^{-1} and D_f is 40–100 μm, as seen in Fig. 3C and D, PFOA have the smaller bubble size, while KPFOS have larger bubble size. For PFOA, the foam approaches equilibrium status at around 15–18 s, whereas the t_e is around 7–10 s for KPFBS. The t_e is increased to around 30 s for PFOA foams with increasing the Q_{air} to 0.6 L min^{-1}, whilst it takes around 12–18 s to reach the equilibrium status for KPFBS foams. In other words, the t_e becomes greater with increasing the Q_{air}. Furthermore, Q_{air} in the studied range has no significant effect on the PFAS foam bubble size. Comparing PFOA and KPFOS results in Fig. 2 and 3, it indicates that smaller bubble size does not necessarily lead to higher foam capacity.

The concentration of PFAS also influences foam structure. Taking the example of KPFOS, the foamability is not linearly correlated with the bulk concentrations. Fig. 4 depicts the foam structure of KPFOS foams with various bulk concentrations, ranging from 0.05 mM to 0.8 mM. A layer of bubbles is obtained when the KPFOS bulk concentrations are 0.01 and 0.02 mM. Nevertheless, the H_f is too small to be recorded. Below 0.01 mM, the KPFOS solutions cannot be foamed. Ranging from 0.01 to 0.4 mM, the foamability is enhanced (*i.e.*, H_f is increased) with increasing the concentration due to the increased KPFOS concentration at the air–water interface.[61,62] Additionally, the bubble size of KPFOS foams becomes more uniform and smaller with an increase in concentration. Increasing the KPFOS concentration beyond 0.4 mM, the bubble size further becomes smaller and more monodispersed.

Published on 23 October 2024. Downloaded on 11/23/2024 3:26:02 AM.

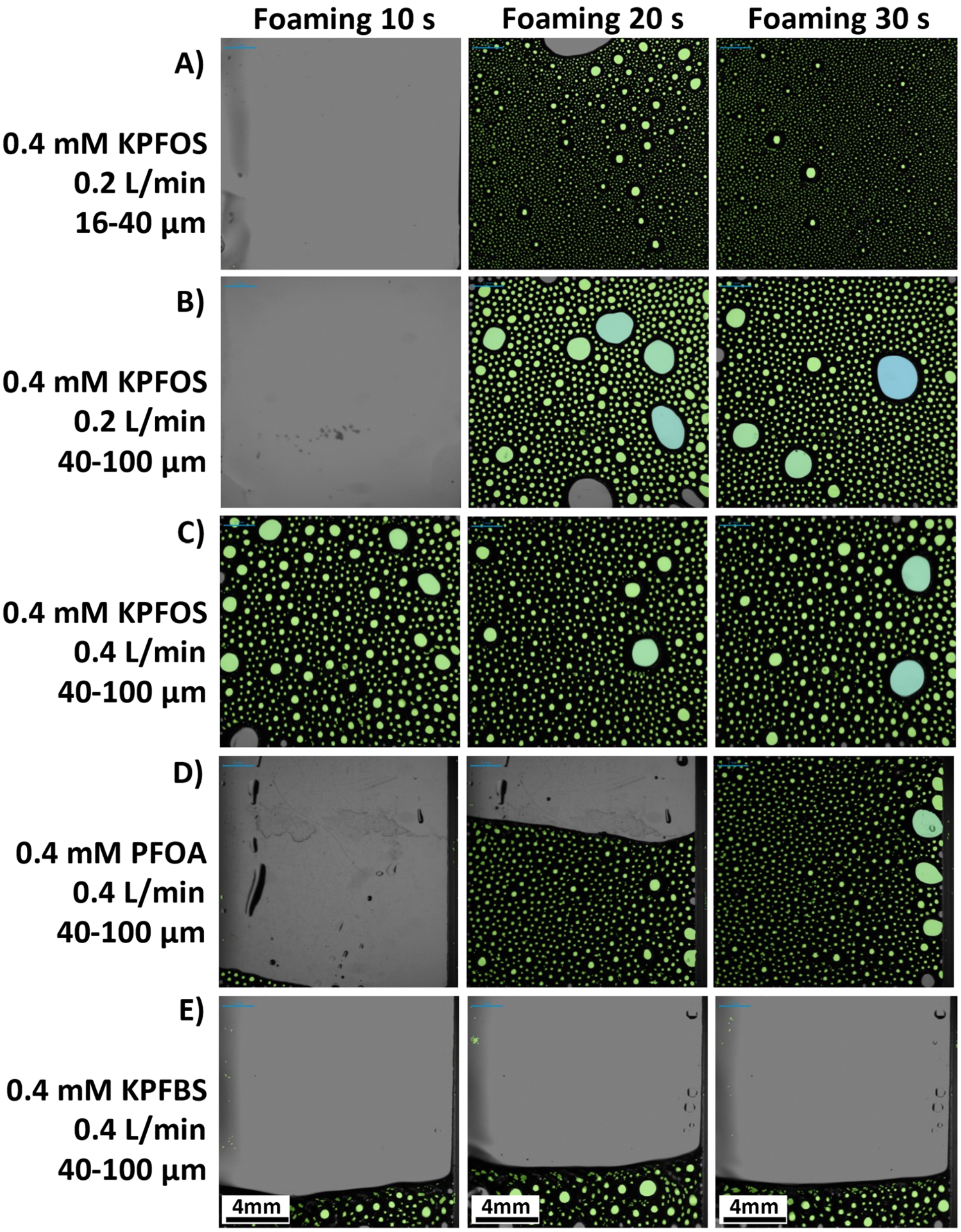

Fig. 3 Foam structure at 10, 20, and 30 s during 30 s of foaming for different PFAS with the same bulk concentration of 0.4 mM by using different aeration conditions. The scale bar is 4 mm. The micrographs show bubbles of 0.4 mM KPFOS aqueous foams by using the air flow rate of 0.2 L min^{-1} and sparged by using the filter with pore size range of (A) 40–100 µm, and (B) 16–40 µm; and bubbles of (C) 0.4 mM KPFOS, (D) 0.4 mM PFOA, and (E) 0.4 mM KPFBS aqueous foams by using air flow rate of 0.4 L min^{-1} and the filter with pore size range of 40–100 µm.

Nonetheless, the H_f is reduced as seen in Fig. 4F. Above 0.8 mM, the foam bubbles cannot be recorded due to the small H_f. Only a thin layer of bubbles is obtained when the concentration is near the KPFOS solubility limit (1.1–1.2 mM) in water. It should be noted that the KPFOS does not reach the critical micelle concentration (CMC) before solubility limit. A similar reduction in foam height by concentration was reported by Behara *et al.*[62] for a mixture of sodium dodecyl benzenesulfonate (DOBS) and sodium lauryl ether sulfate (SLES), which was attributed to the reduction in Gibbs elasticity of the plateau borders.

3.2. Dimensional analysis of foaming behavior: expansion rate of foaming

$\dfrac{H_\text{f}}{H_\text{l}}$ is related to several dimensionless numbers, such as Re and Ca.[52,53,63,64] We consider the equilibrium status of foams for studying $\dfrac{H_\text{f}}{H_\text{l}}$ and use the Buckingham π theorem by listing all independent variables as follows:

$$H_\text{f} = f_1(\rho,\gamma,\eta,\eta_\text{s},E,t_\text{e},Q_\text{air},R,D_\text{c},D_\text{f},H_\text{l},g) \quad (6)$$

Published on 23 October 2024. Downloaded on 11/23/2024 3:26:02 AM.

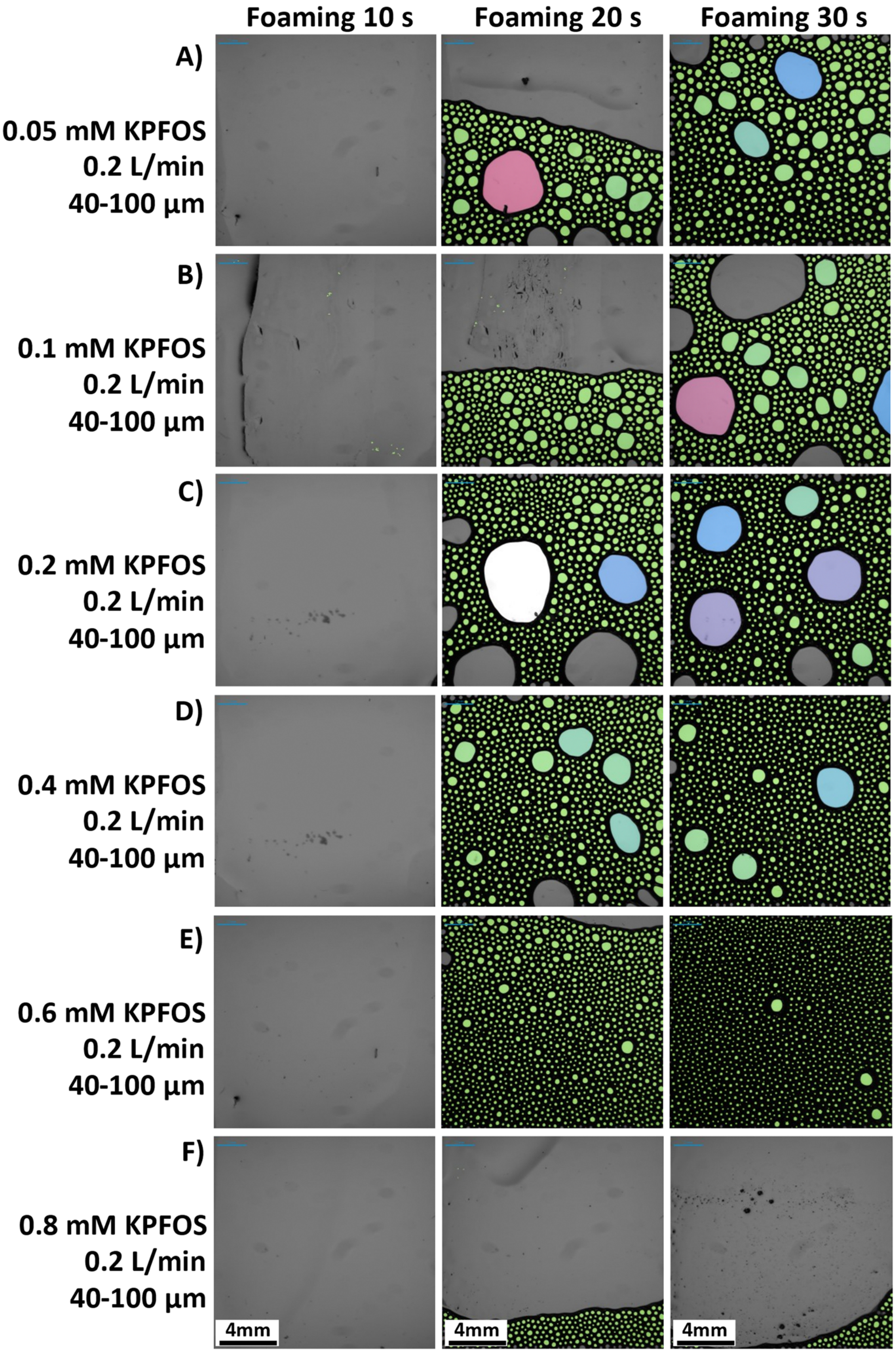

Fig. 4 Foam structure at 10, 20, and 30 s during 30 s of foaming process for (A) 0.05 mM, (B) 0.1 mM, (C) 0.2 mM, (D) 0.4 mM, (E) 0.6 mM, and (F) 0.8 mM KPFOS aqueous foams by using the air flow rate of 0.2 L min^{-1} and the glass filter with pore size range of 40–100 μm. The scale bar is 4 mm. Below 0.05 mM and above 0.8 mM, the foamability is worse and the foam height is not high enough to be captured by the camera.

where ρ is the density of PFAS aqueous solutions, η is the bulk viscosity of PFAS aqueous solutions, D_c is the diameter of the prism column, and g is the gravitational acceleration. The ρ, Q_{air}, and H_{l0} (the initial liquid level) variables are selected as the basic (repeating) variables, which include the basic units of length (m), time (s), and mass (kg). The π groups are determined according to $k = n - m$, where n is the total number of variables and m is the number of basic variables

Published on 23 October 2024. Downloaded on 11/23/2024 3:26:02 AM.

selected in the system. Then eqn (6) becomes:

$$\begin{aligned}\frac{H_\mathrm{f}}{H_\mathrm{l0}} &= f_2\Bigg(\pi_1 = \frac{\gamma}{\rho^1\cdot Q_\mathrm{air}{}^2\cdot H_\mathrm{l0}{}^{-3}},\ \pi_2 = \frac{\eta}{\rho^1\cdot Q_\mathrm{air}{}^1\cdot H_\mathrm{l0}{}^{-1}},\\ &\pi_3 = \frac{\eta_\mathrm{s}}{\rho^1\cdot Q_\mathrm{air}{}^1},\ \pi_4 = \frac{E}{\rho^1\cdot Q_\mathrm{air}{}^2\cdot H_\mathrm{l0}{}^{-3}},\\ &\pi_5 = \frac{t_\mathrm{f}}{Q_\mathrm{air}{}^{-1}\cdot H_\mathrm{l0}{}^3},\ \pi_6 = \frac{R}{H_\mathrm{l0}{}^1},\ \pi_7 = \frac{D_\mathrm{c}}{H_\mathrm{l0}{}^1},\\ &\pi_8 = \frac{D_\mathrm{f}}{H_\mathrm{l0}{}^1},\ \pi_9 = \frac{g}{Q_\mathrm{air}{}^2\cdot H_\mathrm{l0}{}^{-5}}\Bigg)\end{aligned} \tag{7}$$

Eqn (7) can be rearranged by combining variables to form the known dimensionless groups as follows:

$$\begin{aligned}\frac{H_\mathrm{f}}{H_\mathrm{l0}} &= f_3\big(\mathrm{Re_b} = \pi_2{}^{-1}\cdot\pi_7{}^{-2}\cdot\pi_6,\ \mathrm{Ca} = \pi_1{}^{-1}\cdot\pi_2\cdot\pi_7{}^{-2},\\ &\mathrm{We_b} = \pi_1{}^{-1}\cdot\pi_7{}^{-4}\cdot\pi_6,\ \mathrm{Fr_b} = \pi_7{}^{-4}\cdot\pi_9{}^{-1}\cdot\pi_6,\\ &\mathrm{Bq} = \pi_2{}^{-1}\cdot\pi_3\cdot\pi_6{}^{-1}, \Theta = \pi_1\cdot\pi_4{}^{-1},\\ &\zeta_\mathrm{p} = \frac{t_\mathrm{e}}{Q_\mathrm{air}{}^{-1}\cdot H_\mathrm{l0}{}^3}, \frac{R}{H_\mathrm{l0}}, \frac{D_\mathrm{c}}{H_\mathrm{l0}}, \frac{D_\mathrm{f}}{H_\mathrm{l0}}\Big)\end{aligned} \tag{8}$$

where the Reynolds number for the case of bubble rising is $\mathrm{Re_b} = (\rho\cdot Q_\mathrm{air}\cdot R)/(\eta\cdot D_\mathrm{c}{}^2)$, the Capillary number is $\mathrm{Ca} = (Q_\mathrm{air}\cdot\eta)/(\gamma\cdot D_\mathrm{c}{}^2)$, the Weber number for bubble rising is $\mathrm{We_b} = (\rho\cdot Q_\mathrm{air}{}^2\cdot R)/(\gamma\cdot D_\mathrm{c}{}^4)$, the Froude number for bubble rising is $\mathrm{Fr_b} = Q_\mathrm{air}{}^2/(D_\mathrm{c}{}^4\cdot R\cdot g)$, the Boussinesq number is $\mathrm{Bq} = \eta_\mathrm{s}/(\eta\cdot R)$, interface number $\Theta = \gamma/E$ is the ratio of surface tension to dilatational interfacial modulus, and processing number is $\zeta_\mathrm{p} = (t_\mathrm{e}\cdot Q_\mathrm{air})/H_\mathrm{l0}{}^3$. Due to the limited experiments with smaller D_f, only 40–100 μm as the D_f is considered in the dimensional analysis. The eqn (8) can be rewritten as follow:

$$\frac{H_\mathrm{f}}{H_\mathrm{l0}} = f_4\left(\mathrm{Re_b}, \mathrm{Ca}, \mathrm{We_b}, \mathrm{Fr_b}, \mathrm{Bq}, \Theta, \zeta_\mathrm{p}, \frac{R}{H_\mathrm{l0}}, \frac{D_\mathrm{c}}{H_\mathrm{l0}}, \frac{D_\mathrm{f}}{H_\mathrm{l0}}\right) \tag{9}$$

3.2.1. KPFOS aqueous solutions.

The foamability was tested for KPFOS solutions at different concentrations by varying processing parameters of t_f and Q_air. As a result, various t_es are obtained. We used t_e instead of t_f for the dimensional analysis since the equilibrium status was considered. The KPFOS solutions used for the dimensional analysis of $\frac{H_\mathrm{f}}{H_\mathrm{l0}}$ function have no salts added because the steady state cannot be achieved due to the foam overflow. Fig. 5A–G show the effect of various dimensionless numbers on the $\frac{H_\mathrm{f}}{H_\mathrm{l0}}$ of KPFOS foams.

One can see from Fig. 5A, the $\frac{H_\mathrm{f}}{H_\mathrm{l0}}$ is clearly correlated with $\mathrm{Re_b}$. The correlation of $\frac{H_\mathrm{f}}{H_\mathrm{l0}}$ with $\mathrm{Re_b}$ follows Freundlich model (lines in Fig. 5A), and the fitted equations are shown in Table S2 (ESI†). The $\mathrm{Re_b}$ represents the ratio of inertial force and viscous force during bubble rise. The low $\mathrm{Re_b}$ indicates that the flows are laminar, where the viscous force is dominant. This result explains the spherical bubble shape seen in Fig. 3 and 4 as the bubbles will become non-spherical at high $\mathrm{Re_b}$ (>500).[63] A significant increase in $\frac{H_\mathrm{f}}{H_\mathrm{l0}}$ with a decrease in $\mathrm{Re_b}$ is observed for different Q_air. In Bois *et al.*'s work, it was claimed that the lower foaming expansion rate in the high $\mathrm{Re_b}$ regime is due to the transition from intermediate flow to turbulent, where the bubble breakup is easier to take place.[52] However, this is not the case for our system since all PFAS foaming experiments remain in laminar flow. In addition, at the same $\mathrm{Re_b}$, higher Q_air gives rise to higher foamability. Therefore, the observed trend in Fig. 5A is dominated by the bubble size.

The Ca measures the effect of viscous force *versus* interfacial force across the gas–liquid interface. It was reported that the increase of Ca is associated with the change of bubble size and shape. Mary *et al.*[53] used the Ca to predict the R and found the inverse relationship between the bubble size and Ca. Drenckhan *et al.*[64] pointed out that the elongation of bubbles is associated with the greater Ca. Fig. S5 (ESI†) shows the R as a function of Ca. A minimum is observed in R against Ca variation for all three Q_airs. Additionally, a peak is also observed for the relationship between the $\frac{H_\mathrm{f}}{H_\mathrm{l0}}$ and Ca. From our previous work,[24] the highlighted areas in Fig. 5B and Fig. S5 (ESI†) have the highest E, which occurs in the concentration range of 0.2–0.4 mM. Hence, the appearance of $\frac{H_\mathrm{f}}{H_\mathrm{l0}}$ peak and R minimum *versus* Ca coincides with the maximum E.[24] Considering very small Ca in all experiments, the interfacial force dominates the viscous force. According to our previous work, Gibbs adsorption is the dominant mechanism before the maximum, whereas the molecular exchange of PFAS between the interface and bulk prevails on the right side of E maximum.[65] Thus, the correlation between the $\frac{H_\mathrm{f}}{H_\mathrm{l0}}$ of KPFOS and Ca has regime I and II before and after the peak, respectively. In adsorption-dominated regime I, the foamability increases and the bubble size decreases with increasing the Ca, whereas in the molecular exchange-dominated regime II, the foaming behavior becomes worse with increasing the Ca. The equation $y = e^{(ax^2+bx+c)}$ is used to fit the $\frac{H_\mathrm{f}}{H_\mathrm{l0}}$ as a function of Ca, with the fitted equations showing in Table S2 (ESI†). It should be noted that this equation form was used for easing the linearization of final equation. Since $\frac{H_\mathrm{f}}{H_\mathrm{l0}}$ increases with increasing the air injection rates, some data points are not considered for fitting to correctly show the trend. For example, the highlighted points for 0.2 L min^{-1} are excluded (Fig. 5B) since the same concentrations show overflow before reaching the steady state for 0.4 and 0.6 L min^{-1}.

The variation of $\frac{H_\mathrm{f}}{H_\mathrm{l0}}$ against $\mathrm{We_b}$ also follows the Freundlich model as seen in Fig. 5C, and the fitted equations are shown in Table S2 (ESI†). The $\mathrm{We_b}$ is used to determine the significance of foam's inertia in comparison to interfacial forces. As seen, the foamability increases with a decrease in the $\mathrm{We_b}$, thus, the foamability is improved when the effect of interfacial forces becomes more significant than inertia. The $\frac{H_\mathrm{f}}{H_\mathrm{l0}}$ is linearly related to $\mathrm{Fr_b}$ as seen in Fig. 5D. The linear relationships of $\frac{H_\mathrm{f}}{H_\mathrm{l0}}$ as a

This journal is © The Royal Society of Chemistry 2024

Published on 23 October 2024. Downloaded on 11/23/2024 3:26:02 AM.

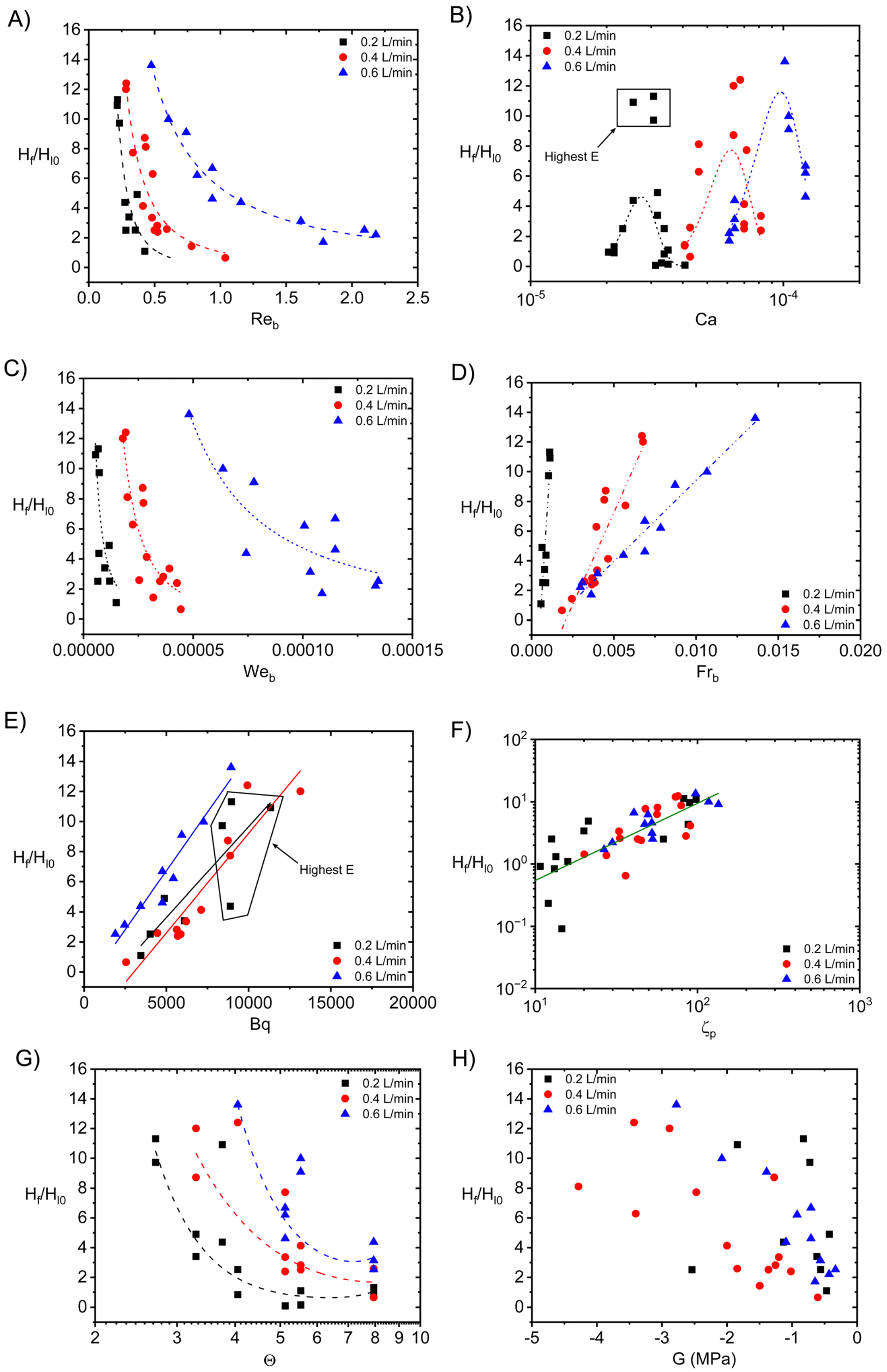

Fig. 5 Evolution of foam expansion rate for KPFOS aqueous solutions with varied concentrations as a function of (A) Reynolds number, (B) Capillary number, (C) Weber number, (D) Froude number, (E) Boussinesq number, (F) processing number, (G) interface number, and (H) Gibbs stability.

Published on 23 October 2024. Downloaded on 11/23/2024 3:26:02 AM.

function of $\mathrm{Fr_b}$ for various Q_{air}s are shown in Table S2 (ESI†). The $\mathrm{Fr_b}$ refers to the ratio of inertial force and gravitational force. In our case, the foaming capacity of KPFOS increases with increasing the effect of inertial force compared to the gravitational force, with this trend being less sharp for higher Q_{air}.

As seen in Fig. 5E and Table S2 (ESI†), $\frac{H_{\mathrm{f}}}{H_{10}}$ is linearly correlated with Bq. The importance of the surface-to-bulk viscous forces is given by the Bq, when the Reynolds number is small.[66] It was reported that the liquid drainage velocity is correlated with the interfacial shear viscosity represented by Bq.[67,68] In this work, since PFAS are small molecules (*i.e.*, soluble surfactants), measuring interfacial shear viscosity is challenging. Thus, we calculated the Bq from the measured interfacial dilatational viscosity. The Bq can also represent the surface mobility since the η_{s} is the effective parameter to characterize the surface mobility.[69] Since E' and η_{s} are related to the surface mobility, the surfactant flow in the plateau borders is regulated by the adsorption behavior occurring at the surface of node.[69] One can see from Fig. 5E that $\frac{H_{\mathrm{f}}}{H_{10}}$ increases with increasing the Bq. For 0.2 L min^{-1}, as pointed in Fig. 5E, the samples having greater values of Bq also have higher E. It can be concluded that the effect of η_{s} on the foaming behavior of KPFOS is significant. Lower $\frac{H_{\mathrm{f}}}{H_{10}}$ obtained for lower η_{s} can be attributed to the increased mobility of molecules at the air–water interface.

As for ζ_{p}, the $\frac{H_{\mathrm{f}}}{H_{10}}$ increases with ζ_{p} due to the increased t_{e} (see Fig. 5F and Table S2, ESI†). The correlation between $\frac{H_{\mathrm{f}}}{H_{10}}$ and Θ was fitted with equation $y = \mathrm{e}^{(ax^2+bx+c)}$, shown as the dashed lines in Fig. 5G (fitted parameters are shown in Table S2, ESI†). Lower Θ, corresponding to better foamability, indicates a lower surface tension and/or higher E influence. The dimensionless numbers that can be analyzed are not limited to the ones mentioned above, but more details will not be discussed in this study.

Gibbs stability can be used as the criterion to determine the stability of air–water interfaces, as suggested for Pickering foams.[44–47] The eqn (10) is originally used to predict bubble coarsening:[70]

$$\frac{\mathrm{d}P}{\mathrm{d}R} = -\frac{2\gamma}{R^2} < 0 \tag{10}$$

where P is the bubble capillary pressure. For the surfactant solutions, eqn (10) is always true since γ is independent of R. This destabilization is to some extent counteracted by introducing the E.[70] Therefore, the eqn (10) becomes:

$$\frac{\mathrm{d}P}{\mathrm{d}R} = -\frac{2\gamma}{R^2} + \frac{4E}{R^2} = G \tag{11}$$

where G is Gibbs stability, and $E > \frac{\gamma}{2}$ is known as the Gibbs stability criterion.[70,71] Fig. 5H shows the $\frac{H_{\mathrm{f}}}{H_{10}}$ *versus* G for KPFOS foams. Negative G implies that the Gibbs stability criterion is not fulfilled for KPFOS foams. Unexpectedly, the foamability decreases as the system is approaching the Gibbs stability criterion, at least for KPFOS aqueous foams without any additives. In other words, since in our system $E < \frac{\gamma}{2}$, when E approaches $\frac{\gamma}{2}$, the interface is more likely to resist against surface area reduction and Ostwald ripening, thus, it is expected that foamability is enhanced. However, this is not the case and as Maestro *et al.*[70] also pointed out, the Gibbs stability criterion is essential to prevent the bubble coarsening, but it is not sufficient to determine the bubble stability.

3.2.2. PFOA aqueous solutions. Given a concentration of PFOA, various concentrations of NaCl were tested. Different t_{e}s are obtained as the processing parameters t_{f} and Q_{air} were varied. The systems reaching steady state are taken into account in this case. Fig. 6A–G show the dependency of $\frac{H_{\mathrm{f}}}{H_{10}}$ on the dimensionless numbers for PFOA. The $\frac{H_{\mathrm{f}}}{H_{10}}$ is negatively correlated with the $\mathrm{Re_b}$ as shown in Fig. 6A. Linear relationships can be used to describe their correlation, and the fitted parameters are shown in Table S3 (ESI†). The $\mathrm{Re_b}$ is smaller than 1.5, confirming the laminar flow. The open points in Fig. 6A are the PFOA foams without adding NaCl, corresponding to low foamability. Nonetheless, the foamability is not linearly increasing with increasing the NaCl concentration. For example, the highest foamability of PFOA is obtained when the NaCl concentration range is 5–50 mM as pointed out in Fig. 6A. Ndiritu *et al.*[72] studied the effect of NaCl on the foamability of cricket proteins, and they found that there is a certain NaCl concentration at which the highest foamability is obtained. They discussed that the increased foamability is due to the enhanced protein solubility, and the further decrease in the foaming capacity is due to the charge-screening and enhanced hydrophobic interaction and intermolecular cohesion between protein molecules.[72,73] Similar explanation may be considered for the foaming of PFOA aqueous solutions.

The peak of $\frac{H_{\mathrm{f}}}{H_{10}}$ as a function of Ca is also observed for PFOA foams containing various concentrations of NaCl (Fig. 6B). The fitting equations for different Q_{air}s are shown in Table S3 (ESI†). We call the NaCl concentration range where the highest foamability over the $\mathrm{Re_b}$ is obtained (as indicated in this figure) as the optimum range. The linear relationship is used to fit with the $\frac{H_{\mathrm{f}}}{H_{10}}$ as a function of $\mathrm{We_b}$, and the fitted equations are shown in Table S3 (ESI†). When the NaCl concentration is in between 5–50 mM, smaller $\mathrm{We_b}$s and higher $\frac{H_{\mathrm{f}}}{H_{10}}$ ratios are obtained.

A single equation can be used to describe the relationship between the and $\mathrm{Fr_b}$ for all PFOA samples as seen in Fig. 6D (see Table S3, ESI†). At a certain point, the effect of inertial force with respect of gravitational force on PFOA foamability is no longer significant as $\frac{H_{\mathrm{f}}}{H_{10}}$ is reaching a plateau. While the highest Bq (largest η_{s}) corresponds to the optimized NaCl concentration range, the $\frac{H_{\mathrm{f}}}{H_{10}}$ does not show a considerable

Published on 23 October 2024. Downloaded on 11/23/2024 3:26:02 AM.

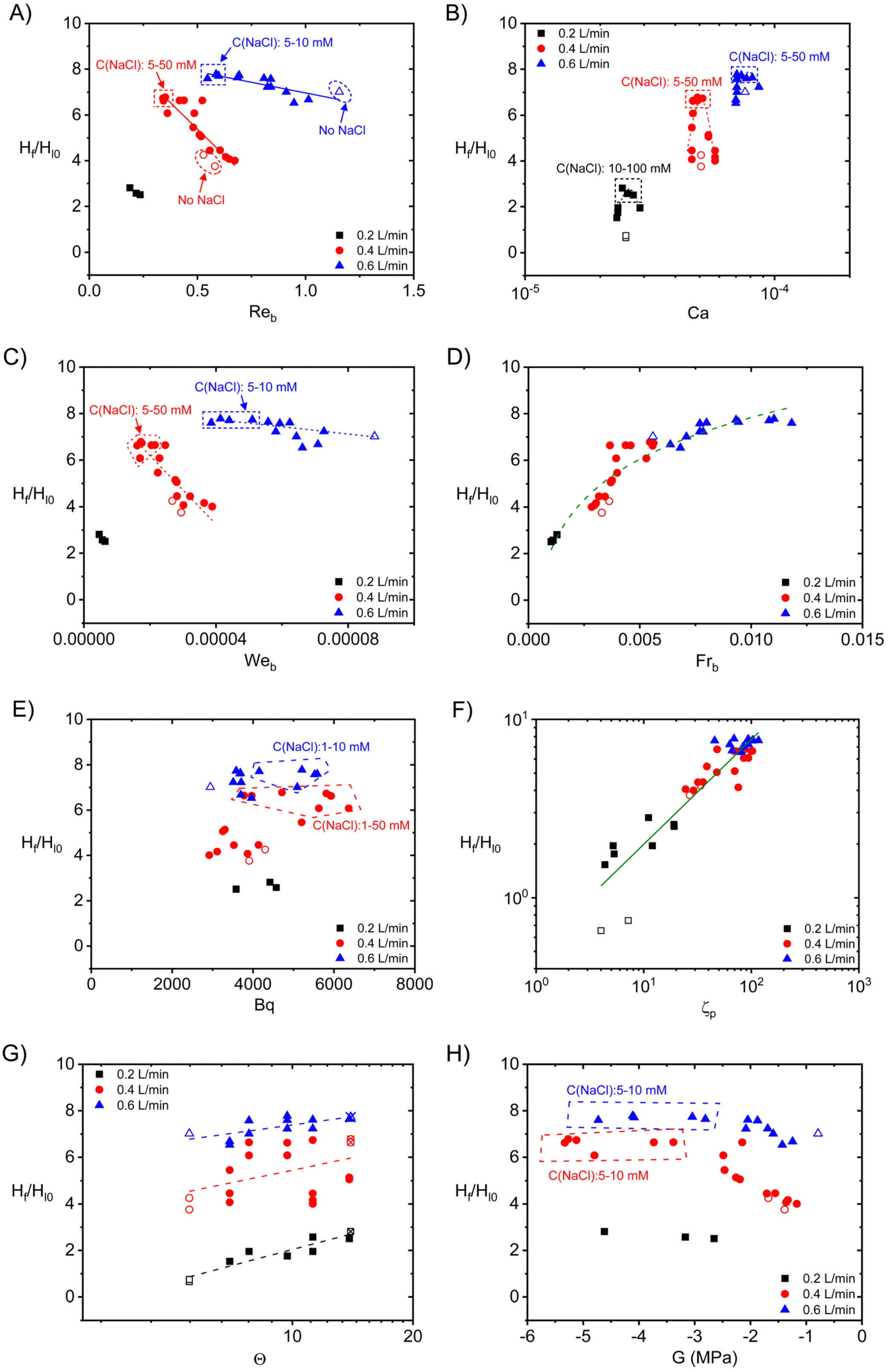

Fig. 6 Evolution of foam expansion rate for 0.4 mM PFOA aqueous solutions containing different concentrations of NaCl as a function of (A) Reynolds number, (B) Capillary number, (C) Weber number, (D) Froude number, (E) Boussinesq number, (F) processing number, (G) interface number, and (H) Gibbs stability. The unfilled markers are for the PFOA foams without NaCl.

Published on 23 October 2024. Downloaded on 11/23/2024 3:26:02 AM.

dependence on the Bq (Fig. 6E). Addition of NaCl increases the ζ_p (Fig. 6F and Table S3, ESI†) due to the enhanced t_e. However, the dependency of $\frac{H_f}{H_{l0}}$ on the ζ_p becomes less significant for higher Q_{air}. In the case of Θ, the $\frac{H_f}{H_{l0}}$ increases with Θ in the 6–14 range, which is unexpected since higher Θ means higher surface tension or lower interfacial modulus. The crossed points in Fig. 6G have the NaCl concentration of 10 mM, above which the foamability decreases (solid points refer to the other NaCl concentrations, both lower and higher than 10 mM).

Fig. 6H depicts the $\frac{H_f}{H_{l0}}$ against G. The G is still negative for PFOA foams with and without NaCl. Therefore, the Gibbs criterion is not fulfilled within the studied regime for PFOA. Additionally, adding NaCl reduces the G, but the foamability increases. Also, the foamability is independent of the G within the optimum NaCl concentrations as highlighted in Fig. 6H. In the case of non-optimum NaCl concentrations, as the E is getting closer to $\frac{\gamma}{2}$, the foaming capacity is somewhat hindered. The results suggest the significance of colloidal forces between bubbles, which is not considered in Gibbs criterion.

3.2.3. KPFBS aqueous solutions.

The foaming capacity of KPFBS is weaker compared to that of KPFOS and PFOA at the same molarity. Even for Q_{air} of 0.4 L min^{-1}, only top part of the foams can be recorded by camera. Therefore, the KPFBS foams obtained by the Q_{air} of 0.6, 0.8 and 1.0 L min^{-1} are studied. The KPFBS foams in steady state are presented. $CaCl_2$ salt was added to the KPFBS foams because the sulfonic acid group is observed to form complex structure in the presence of divalent salts according to our study (to be published separately). Only two concentrations of $CaCl_2$ were tested to qualitatively compare the effect of high and low $CaCl_2$ concentration. Fig. 7A–F show the dependency of $\frac{H_f}{H_{l0}}$ on various dimensionless numbers for KPFBS. We observe similar correlations between $\frac{H_f}{H_{l0}}$ and Re_b, Ca, We_b, Fr_b, and ζ_p for KPFBS similar to that of KPFOS and PFOA. As an example in Fig. 7A, the $\frac{H_f}{H_{l0}}$ decreases when the effect of inertial force becomes more significant. Since the data points are to some extent superimposed, one equation can be used to describe the relationship as seen in Table S4 (ESI†). Additionally, the introduction of $CaCl_2$ does not remarkably enhance the foamability of KPFBS. However, higher concentrations of $CaCl_2$, such as 100 mM, tend to weaken the foaming capacity of KPFBS and increase the Re_b as highlighted in Fig. 7A.

In Fig. 7B, 0.2 and 0.4 L min^{-1} were also included to determine the relationship between the $\frac{H_f}{H_{l0}}$ and Ca since bubble size is not required (it should be noted that if the foam height does not reach the camera's field of view, the bubble size data is not available). The fitted equations are shown in Table S4 (ESI†). Due to the limited concentrations of either KPFBS or $CaCl_2$, the R^2 is reduced. However, the peaks of $\frac{H_f}{H_{l0}}$ are still appearing. Moreover, the addition of $CaCl_2$ increases the Ca for KPFBS foams, revealing that the viscous force effect becomes more important. In Fig. 7C, the Freundlich model was used to describe the correlation between the $\frac{H_f}{H_{l0}}$ and We_b, for which the equations are shown in Table S4 (ESI†). The linear relationships between the $\frac{H_f}{H_{l0}}$ and Fr_b for 0.6, 0.8, and 1.0 L min^{-1} are shown in Table S4 (ESI†) and Fig. 7D. The foaming capacity decreases with increasing the We_b and Fr_b. Furthermore, higher concentration of $CaCl_2$ tend to enhance the We_b and reduce the Fr_b, and at the same time, the foamability is hindered.

From our previous work,[24] dilatational interfacial rheology of 0.4 mM of KPFBS could not be measured due to its high solubility and weaker amphiphilicity, thus, the E is not considered. Hence, the Bq and Θ are not discussed for KPFBS foams. No significant influence of adding $CaCl_2$ on ζ_p is observed according to Fig. 7E, although the $\frac{H_f}{H_{l0}}$ increases with increasing the ζ_p (Table S4, ESI†). The more scattered points in Fig. 7E compared to KPFOS results can be due to the worst foamability of short-chain KPFBS. In other words, the KPFBS foams always have a relatively poorer quality in terms of bubble imaging due to the fastest bubble film rupture. However, the effect of processing on KPFBS foams is still significant. In addition, similar to KPFOS and PFOA systems, the $\frac{H_f}{H_{l0}}$ is reduced as KPFBS samples reach the Gibbs stability criterion. Also, adding $CaCl_2$ does not dramatically enhance or decrease the G as shown in Fig. 7E. Nonetheless, if only considering the KPFBS foams with $CaCl_2$, higher $CaCl_2$ concentrations (100 mM) qualitatively make the systems approach the Gibbs stability criterion.

3.2.4. Prediction of foaming expansion rate.

The concentration of PFAS solutions is far below than their critical micelle concentration (CMC);[24] therefore, ρ and η are taken as the values of pure water, remaining constants. In addition, D_c, H_{l0}, and D_f are also taken as the constants, thus, $\frac{D_c}{H_{l0}}$ and $\frac{D_f}{H_{l0}}$ remain constant. Generally, the dimensionless numbers of Re_b, Fr_b, ζ_p, and $\frac{R}{H_{l0}}$ represent the processing parameters, while Ca, We_b, Bq, and Θ indicate the effect of interfacial properties. Consequently, the eqn (9) can be simplified as follow:

$$\frac{H_f}{H_{l0}} = f_5\left(Re_b, Ca, We_b, Fr_b, Bq, \Theta, \zeta_p, \frac{R}{H_{l0}}\right) \tag{12}$$

The eqn (12) can be written, for example, as the monomial form shown below:

$$\frac{H_f}{H_{l0}} = C_0 \cdot Re_b^a \cdot e^{\left(b1\cdot Ca^2 + b2\cdot Ca\right)} \cdot We_b^c \cdot Fr_b^d \cdot Bq^e \cdot e^{\left(f1\cdot\Theta^2 + f2\cdot\Theta\right)} \cdot \zeta_p^g \cdot \left(\frac{R}{H_{l0}}\right)^h \tag{13}$$

where C_0, a, $b1$, $b2$, c, d, e, $f1$, $f2$, g, and h are constants. The data were fitted to obtain the constants. More details about acquiring the coefficients can be found in the ESI.† Data in Table S5 (ESI†) were used to fit the eqn (13) and identify the proper coefficients for KPFOS solutions. The fitted values for eqn (13)

Published on 23 October 2024. Downloaded on 11/23/2024 3:26:02 AM.

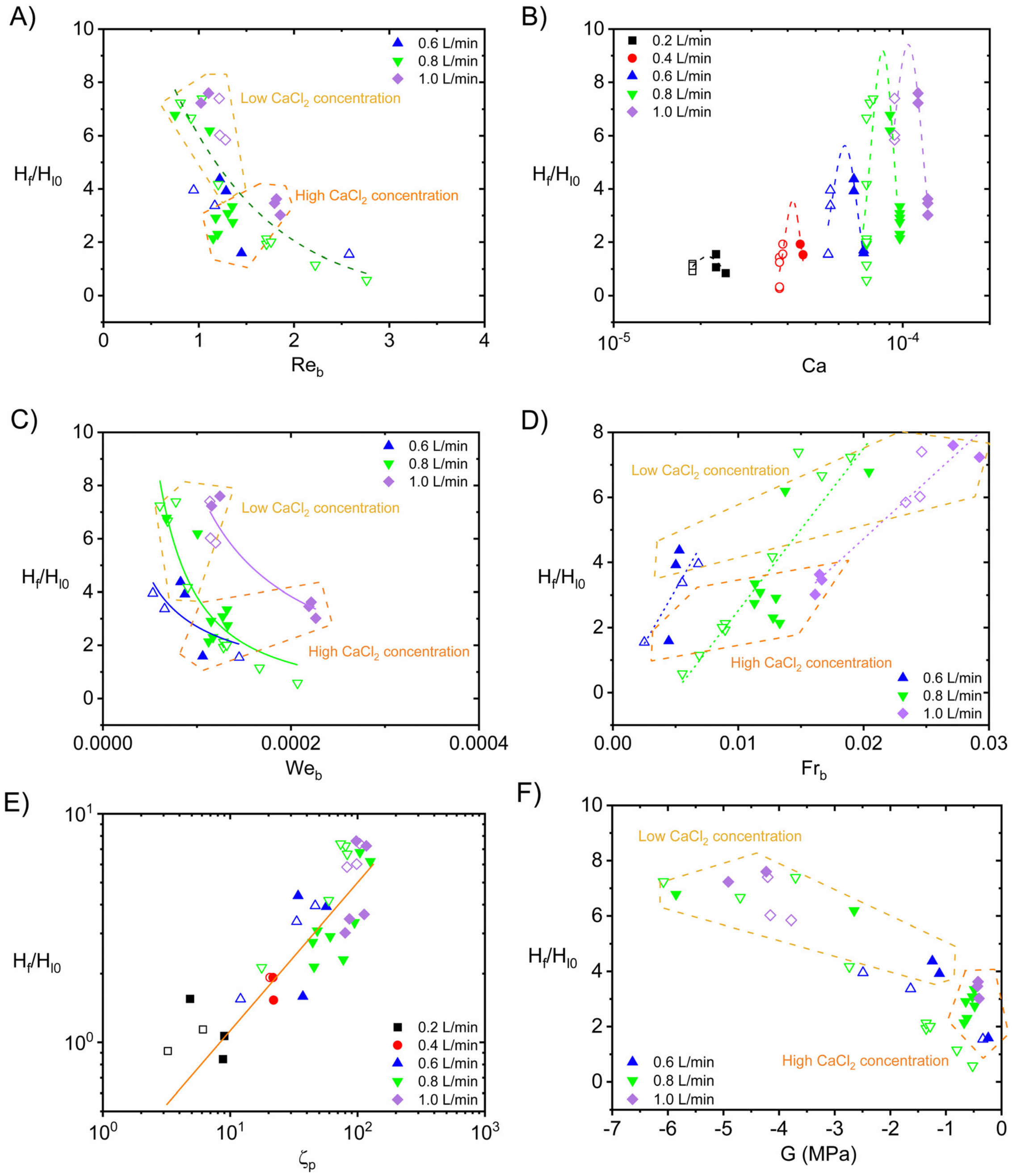

Fig. 7 Evolution of foam expansion rate for KPFBS aqueous solutions containing $CaCl_2$ as a function of (A) Reynolds number, (B) Capillary number, (C) Weber number, (D) Froude number, (E) processing number, and (F) Gibbs stability. The filled markers are the KPFBS foams containing $CaCl_2$, and the unfilled ones are for the foams without $CaCl_2$.

are in good agreement with the experimental values as shown in Fig. S6 (ESI†), resulting in:

$$\frac{H_f}{H_{l0}} = 1587.63 \cdot \mathrm{Re_b}^{-1.72} \cdot e^{\left(-9.00\times10^{7}\cdot \mathrm{Ca}^2+2.00\times10^{4}\cdot \mathrm{Ca}\right)} \cdot \mathrm{We_b}^{-0.44} \cdot \mathrm{Fr_b}^{1.02} \cdot \mathrm{Bq}^{0.72} \cdot e^{\left(0.097\cdot\Theta^2-1.07\cdot\Theta\right)} \cdot {\zeta_p}^{0.45} \cdot \left(\frac{R}{H_{l0}}\right)^{2.85} \tag{14}$$

with a R^2 of 0.86605, suggesting that the experimental values are reasonably fitted with the model.

The foamability of KPFOS is affected by all dimensionless numbers, but one should notice that the relatively larger power coefficients of $\mathrm{Re_b}$ and $\frac{R}{H_{l0}}$ in eqn (14) suggest the relatively more significant influence of $\mathrm{Re_b}$ and R on the foamability of KPFOS in the studied concentration range. The Q_{air} and R have the major effects on the expansion rate of KPFOS foams, and both Q_{air} and R influence the $\mathrm{Re_b}$. Additionally, the $\mathrm{We_b}$ and $\mathrm{Fr_b}$

Published on 23 October 2024. Downloaded on 11/23/2024 3:26:02 AM.

Table 3 Correlation between the PFAS foaming behavior and dimensionless numbers

	KPFOS aqueous foams		PFOA aqueous foams		KPFBS aqueous foams
Dimensionless number	Foaming expansion rate	Significance	Foaming expansion rate	Significance	Foaming expansion rate
$\mathrm{Re_b}$	✓	5	✗	—	✗
Ca	✓	6	✓	5	✓
$\mathrm{We_b}$	✓	**3**	✗	—	✗
$\mathrm{Fr_b}$	✓	**2**	✓	**1**	✓
Bq	✓	**1**	✓	**2**	✗
Θ	✓	4	✓	4	✗
ζ_p	✓	7	✓	**3**	✓
$\frac{R}{H_{l0}}$	✓	—	✓	—	✗

also contain Q_{air} and R, and higher coefficients for $\mathrm{Re_b}$ and $\mathrm{Fr_b}$ suggest that the inertial force effect is significant for KPFOS foamability. Moreover, comparing $\mathrm{We_b}$ to Bq, higher coefficient for Bq suggests that the interfacial viscosity affects the KPFOS foamability much more than expected. The tick marks in Table 3 indicate whether a dimensionless number significantly contributes to the foaming behavior. Given the range of dimensionless numbers according to Fig. 5, we can further estimate the influence of each number on the KPFOS foamability. For example, the $\mathrm{Re_b}$ ranges from 0.2 to 2.2, giving the $\mathrm{Re_b}^{-1.72}$ range between 0.26 and 15.93. If the range is close to 1, the effect will be negligible. Also, the numbers in Table 3 rank the effect of each dimensionless number.

For PFOA, as shown in Fig. S7 (ESI†), the R^2 of the fit (R^2 = 0.96797) to eqn (13) based on Table S6 (ESI†) implies good agreement between the model values and experimental values of $\frac{H_f}{H_{l0}}$ with following equation:

$$\frac{H_f}{H_{l0}} = 3.06 \cdot e^{\left(-1.00\times10^8\cdot\mathrm{Ca}^2+1.00\times10^4\cdot\mathrm{Ca}\right)} \cdot \mathrm{Fr_b}^{0.41} \cdot \mathrm{Bq}^{0.38} \cdot \Theta^{0.26} \cdot {\zeta_p}^{0.16} \cdot \left(\frac{R}{H_{l0}}\right)^{0.42} \tag{15}$$

The coefficients of $\mathrm{Re_b}$ and $\mathrm{We_b}$ are small and can be estimated as zero without affecting the R^2. The greater coefficients of $\mathrm{Fr_b}$ and $\frac{R}{H_{l0}}$ in eqn (15) reveal that the foamability of PFOA in the presence of NaCl highly depends on the Q_{air} and R. Table 3 shows that the addition of NaCl improves the foamability of PFOA through affecting the interfacial properties, represented by Bq. Fig. S8 (ESI†) shows the prediction of foaming capacity for KPFBS solutions with a R^2 of 0.73937. One of the possible reasons for the lower R^2 of fitting for KPFBS foaming behavior could be the absence of Θ and Bq experimental values for dimensional analysis. It might also be due to the weak adsorption activity of KPFBS.[24] The monomial equation is shown below:

$$\frac{H_f}{H_{l0}} = 12.30 \times e^{\left(-4.00\times10^7\times\mathrm{Ca}^2\right)} \times \mathrm{Fr_b}^{0.51} \times {\zeta_p}^{0.37} \tag{16}$$

The case of KPFBS is simple, and the foamability only depends on three dimensionless numbers of Ca, $\mathrm{Fr_b}$, and ζ_p. The dependency of expansion rate of KPFBS foaming on R (*i.e.*, $\frac{R}{H_{l0}}$) in this study is not significant. Table S7 (ESI†) summarizes the universal equations for the studied PFAS foams.

4. Conclusions

In this present study, the foaming behavior of three PFAS, which are KPFOS, PFOA and KPFBS, is studied by aerating their aqueous solutions with varied processing parameters of air flow rate and foaming time. Generally, the foaming capacity follows the order of KPFOS > PFOA > KPFBS. The foaming capacity of KPFOS, PFOA and KPFBS is further investigated by using dimensional analysis approach to correlate the expansion rate of foaming with several different dimensionless numbers.

PFAS bulk concentration affects their foaming behavior. Taking the example of KPFOS, there is a concentration (around 0.4 mM) at which the highest foam height is obtained. However, the bubble size continuously decreases with increasing the bulk concentration. Both processing and interfacial parameters influence KPFOS foamability with the Boussinesq number affecting the expansion rate of foaming the most in the studied regime. The addition of salt, NaCl, and its concentration affects PFOA foaming behavior. The NaCl concentration range of 5–50 mM improves PFOA foaming capacity by influencing the Boussinesq number. Interestingly, the maximum value of foam height with changing the Capillary number and interface number appear around this NaCl concentration range. The situation of KPFBS is much simpler. According to our previous study, 0.4 mM KPFBS has negligible dilatational interfacial modulus. Therefore, Boussinesq and interface numbers could not be considered for KPFBS. The foaming expansion rate for KPFBS is governed by the Froude number. Our study suggests that lower $\mathrm{CaCl_2}$ concentration is helpful to obtain the relatively higher foaming expansion rate for short-chain PFAS, coinciding with lower Reynolds and Weber numbers, as well as Gibbs stability. Nevertheless, the lower accuracy of the fit for KPFBS foaming expansion rate suggests the significant role of PFAS interfacial properties when predicting their foaming properties.

Compared to the processing parameters, our study demonstrates the significant impact of interfacial properties, representing by Capillary, Weber, Boussinesq and interface numbers on foaming behavior, which could be also the case of other surfactants. A maximum PFAS foaming capacity with changing

This journal is © The Royal Society of Chemistry 2024

Published on 23 October 2024. Downloaded on 11/23/2024 3:26:02 AM.

the Capillary number is observed, coinciding with the appearance of highest dilatational interfacial modulus. In this work, the interfacial rheology parameters are for the first time considered for performing the dimensional analysis on foaming of surfactant solutions, providing an insight into the scale-up of foam fractionation for removal of emerging contaminants. Moreover, the Gibbs criterion is not fulfilled, implying the PFAS foams are relatively unstable, which may be beneficial in real application since the collected foam after fractionation should be destabilized for chemical degradation of PFAS.

Finally, the models for different PFAS do not superimpose, likely due to the lack of data accounting for bubble interactions and foam thin film behavior. Therefore, further studies are needed to incorporate these effects and move towards a universal model.

Data availability

The data supporting this article have been included as part of the ESI.†

Conflicts of interest

There are no conflicts to declare.

Acknowledgements

The Bureau of Reclamation (BoR) provided financial support for this work under the Grant of R21AC10418-00. The authors also thank the Institute for Applied Surfactant Research (IASR) for providing instruments used in this work.

References

1 J. Glüge, M. Scheringer and I. T. Cousins, *et al.*, An overview of the uses of per- And polyfluoroalkyl substances (PFAS), *Environ. Sci.: Processes Impacts*, 2020, **22**(12), 2345–2373, DOI: **10.1039/d0em00291g**.

2 S. Kurwadkar, J. Dane and S. R. Kanel, *et al.*, Per- and polyfluoroalkyl substances in water and wastewater: A critical review of their global occurrence and distribution, *Sci. Total Environ*, 2022, **809**, 151003, DOI: **10.1016/j.scitotenv.2021.151003**.

3 Z. Zhang, D. Sarkar, J. K. Biswas and R. Datta, Biodegradation of per- and polyfluoroalkyl substances (PFAS): A review, *Bioresour. Technol.*, 2022, **344**, 126223, DOI: **10.1016/j.biortech.2021.126223**.

4 J. Li, J. Sun and P. Li, Exposure routes, bioaccumulation and toxic effects of per- and polyfluoroalkyl substances (PFASs) on plants: A critical review, *Environ. Int.*, 2022, **158**, 106891, DOI: **10.1016/j.envint.2021.106891**.

5 B. Trang, Y. Li, X.-S. Xue, M. Ateia, K. N. Houk and W. R. Dichtel, Low-temperature mineralization of perfluorocarboxylic acids, *Science*, 2022, **377**(6608), 839–845, DOI: **10.1126/science.abm8868**.

6 A. B. Nienhauser, M. S. Ersan, Z. Lin, F. Perreault, P. Westerhoff and S. Garcia-Segura, Boron-doped diamond electrodes degrade short- and long-chain per- and polyfluorinated alkyl substances in real industrial wastewaters, *J. Environ. Chem. Eng.*, 2022, **10**(2), 107192, DOI: **10.1016/j.jece.2022.107192**.

7 X. Liu, X. Zheng and L. Zhang, *et al.*, Joint Toxicity Mechanisms of Binary Emerging Pfas Mixture on Algae (Chlorella Pyrenoidosa) at Environmental Concentration, *J. Hazard. Mater.*, 2022, **437**, 129355, DOI: **10.2139/ssrn.4063771**.

8 P. Pierozan, M. Kosnik and O. Karlsson, High-content analysis shows synergistic effects of low perfluorooctanoic acid (PFOS) and perfluorooctane sulfonic acid (PFOA) mixture concentrations on human breast epithelial cell carcinogenesis, *Environ. Int.*, 2023, **172**, 107746, DOI: **10.1016/j.envint.2023.107746**.

9 B. P. Rickard, I. Rizvi and S. E. Fenton, Per- and poly-fluoroalkyl substances (PFAS) and female reproductive outcomes: PFAS elimination, endocrine-mediated effects, and disease, *Toxicology*, 2022, **465**, 153031, DOI: **10.1016/j.tox.2021.153031**.

10 T. G. Ambaye, M. Vaccari, S. Prasad and S. Rtimi, Recent progress and challenges on the removal of per- and polyfluoroalkyl substances (PFAS) from contaminated soil and water, *Environ. Sci. Pollut. Res.*, 2022, **29**(39), 58405–58428, DOI: **10.1007/s11356-022-21513-2**.

11 S. E. Fenton, A. Ducatman and A. Boobis, *et al.*, Per- and Polyfluoroalkyl Substance Toxicity and Human Health Review: Current State of Knowledge and Strategies for Informing Future Research, *Environ. Toxicol. Chem.*, 2021, **40**(3), 606–630, DOI: **10.1002/etc.4890**.

12 E. M. Sunderland, X. C. Hu, C. Dassuncao, A. K. Tokranov, C. C. Wagner and J. G. Allen, A review of the pathways of human exposure to poly- and perfluoroalkyl substances (PFASs) and present understanding of health effects, *J. Exposure Sci. Environ. Epidemiol.*, 2019, **29**(2), 131–147, DOI: **10.1038/s41370-018-0094-1**.

13 M. N. Ehsan, M. Riza, M. N. Pervez, M. M. O. Khyum, Y. Liang and V. Naddeo, Environmental and health impacts of PFAS: Sources, distribution and sustainable management in North Carolina (USA), *Sci. Total Environ.*, 2023, **878**, 163123, DOI: **10.1016/j.scitotenv.2023.163123**.

14 S. Y. Wee and A. Z. Aris, Revisiting the ‘‘forever chemicals’’, PFOA and PFOS exposure in drinking water, *npj Clean Water*, 2023, **6**(1), 57, DOI: **10.1038/s41545-023-00274-6**.

15 B. E. Blake and S. E. Fenton, Early life exposure to per- and polyfluoroalkyl substances (PFAS) and latent health outcomes: A review including the placenta as a target tissue and possible driver of peri- and postnatal effects, *Toxicology*, 2020, **443**, 152565, DOI: **10.1016/j.tox.2020.152565**.

16 B. C. Crone, T. F. Speth and D. G. Wahman, *et al.*, Occurrence of per- and polyfluoroalkyl substances (PFAS) in source water and their treatment in drinking water, *Crit. Rev. Environ. Sci. Technol.*, 2019, **49**(24), 2359–2396, DOI: **10.1080/10643389.2019.1614848**.

17 X. C. Hu, D. Q. Andrews and A. B. Lindstrom, *et al.*, Detection of Poly- and Per fl uoroalkyl Substances (PFASs)

Published on 23 October 2024. Downloaded on 11/23/2024 3:26:02 AM.

in U.S. Drinking Water Linked to Industrial Sites, Military Fire Training Areas, and Wastewater Treatment Plants, *Environ. Sci. Technol. Lett.*, 2016, **3**(10), 344–350, DOI: 10.1021/acs.estlett.6b00260.

18 PFAS National Primary Drinking Water Regulation. US EPA.:40 CFR Parts 141 and 142, https://www.federalregister.gov/d/2024-07773.

19 E. Tavasoli, J. L. Luek, J. P. Malley and P. J. Mouser, Distribution and fate of per- And polyfluoroalkyl substances (PFAS) in wastewater treatment facilities, *Environ. Sci.: Processes Impacts*, 2021, **23**(6), 903–913, DOI: 10.1039/d1em00032b.

20 S. Barisci and R. Suri, Occurrence and removal of poly/perfluoroalkyl substances (PFAS) in municipal and industrial wastewater treatment plants, *Water Sci. Technol.*, 2021, **84**(12), 3442–3468, DOI: 10.2166/wst.2021.484.

21 S. Liu, B. Jin, H. P. H. Arp, W. Chen, Y. Liu and G. Zhang, The Fate and Transport of Chlorinated Polyfluorinated Ether Sulfonates and Other PFAS through Industrial Wastewater Treatment Facilities in China, *Environ. Sci. Technol.*, 2022, **56**(5), 3002–3010, DOI: 10.1021/acs.est.1c04276.

22 P. H. N. Vo, T. Buckley, X. Xu, T. M. H. Nguyen, V. Rudolph and P. Shukla, Foam fractionation of per- and polyfluoroalkyl substances (PFASs) in landfill leachate using different cosurfactants, *Chemosphere*, 2023, **310**, 136869, DOI: 10.1016/j.chemosphere.2022.136869.

23 S. J. Smith, C. Keane, L. Ahrens and K. Wiberg, Integrated Treatment of Per- and Polyfluoroalkyl Substances in Existing Wastewater Treatment Plants—Scoping the Potential of Foam Partitioning, *ACS ES&T Eng.*, 2023, **3**(9), 1276–1285, DOI: 10.1021/acsestengg.3c00091.

24 M. Zhou, Z. Abbasian Chaleshtari, B.-J. Shiau, B. P. Grady and R. Foudazi, Air-water interfacial properties of perfluorosulfonic acid salts with different chain lengths, *Colloids Surf., A*, 2024, **694**, 134129, DOI: 10.1016/j.colsurfa.2024.134129.

25 Z. Abbasian Chaleshtari and R. Foudazi, A Review on Per-and Polyfluoroalkyl Substances (PFAS) Remediation: Separation Mechanisms and Molecular Interactions, *ACS ES&T Water*, 2022, **2**(12), 2258–2272, DOI: 10.1021/acsestwater.2c00271.

26 Pennsylvania DEP. PFAS Action Team; Pennsylvania's Department of Environmental Protection, 2019, https://files.dep.state.pa.us/Water/DrinkingWater/PerfluorinatedChemicals/Reports/20191205-PFAS-Action-Team-Initial-Report-Pennsylvania.pdf.

27 Y. Lyu, M. L. Brusseau, W. Chen, N. Yan, X. Fu and X. Lin, Adsorption of PFOA at the Air-Water Interface during Transport in Unsaturated Porous Media, *Environ. Sci. Technol.*, 2018, **52**(14), 7745–7753, DOI: 10.1021/acs.est.8b02348.

28 T. Buckley, X. Xu, V. Rudolph, M. Firouzi and P. Shukla, Review of foam fractionation as a water treatment technology, *Sep. Sci. Technol.*, 2022, **57**(6), 929–958, DOI: 10.1080/01496395.2021.1946698.

29 N. Pal, N. Kumar, A. Verma, K. Ojha and A. Mandal, Performance Evaluation of Novel Sunflower Oil-Based Gemini Surfactant(s) with Different Spacer Lengths: Application in Enhanced Oil Recovery, *Energy Fuels*, 2018, **32**(11), 11344–11361, DOI: 10.1021/acs.energyfuels.8b02744.

30 N. Pal, A. Verma, K. Ojha and A. Mandal, Nanoparticle-modified gemini surfactant foams as efficient displacing fluids for enhanced oil recovery, *J. Mol. Liq.*, 2020, **310**, 113193, DOI: 10.1016/j.molliq.2020.113193.

31 S. Shetty, I. V. Chernyshova and S. Ponnurangam, Foam flotation of rare earth elements by conventional and green surfactants, *Miner. Eng.*, 2020, **158**, 106585, DOI: 10.1016/j.mineng.2020.106585.

32 W. Zhang and R. Honaker, A fundamental study of octanohydroxamic acid adsorption on monazite surfaces, *Int. J. Miner. Process.*, 2017, **164**, 26–36, DOI: 10.1016/j.minpro.2017.05.006.

33 C. Marion, R. Li and K. E. Waters, A review of reagents applied to rare-earth mineral flotation, *Adv. Colloid Interface Sci.*, 2020, **279**, 102142, DOI: 10.1016/j.cis.2020.102142.

34 P. Meng, S. Deng and A. Maimaiti, *et al.*, Efficient removal of perfluorooctane sulfonate from aqueous film-forming foam solution by aeration-foam collection, *Chemosphere*, 2018, **203**, 263–270, DOI: 10.1016/j.chemosphere.2018.03.183.

35 S. J. Smith, K. Wiberg, P. McCleaf and L. Ahrens, Pilot-Scale Continuous Foam Fractionation for the Removal of Per- and Polyfluoroalkyl Substances (PFAS) from Landfill Leachate, *ACS Environ. Sci. Technol. Water*, 2022, **2**(5), 841–851, DOI: 10.1021/acsestwater.2c00032.

36 Y. Wang, Y. Ji, V. Tishchenko and Q. Huang, Removing per- and polyfluoroalkyl substances (PFAS) in water by foam fractionation, *Chemosphere*, 2023, **311**, 137004, DOI: 10.1016/j.chemosphere.2022.137004.

37 D. J. Burns, P. Stevenson and P. J. C. Murphy, PFAS removal from groundwaters using Surface-Active Foam Fractionation, *Remediation*, 2021, **31**(4), 19–33, DOI: 10.1002/rem.21694.

38 D. J. Burns, H. M. Hinrichsen, P. Stevenson and P. J. C. Murphy, Commercial-scale remediation of per- and polyfluoroalkyl substances from a landfill leachate catchment using Surface-Active Foam Fractionation (SAFF®), *Remediation*, 2022, **32**(3), 139–150, DOI: 10.1002/rem.21720.

39 Y. C. Lee, P. Y. Wang, S. L. Lo and C. P. Huang, Recovery of perfluorooctane sulfonate (PFOS) and perfluorooctanoate (PFOA) from dilute water solution by foam flotation, *Sep. Purif. Technol.*, 2017, **173**, 280–285, DOI: 10.1016/j.seppur.2016.09.012.

40 H. B. Lamichhane and D. W. M. Arrigan, Electroanalytical chemistry of per- and polyfluoroalkyl substances, *Curr. Opin. Electrochem.*, 2023, **40**, 101309, DOI: 10.1016/j.coelec.2023.101309.

41 S. Mahpishanian, M. Zhou and R. Foudazi, Magnetic amino-functionalized graphene oxide nanocomposite for PFAS removal from water, *Environ. Sci. Adv.*, 2024, DOI: 10.1039/d4va00171k.

42 D. Beneventi, B. Carre and A. Gandini, Role of surfactant structure on surface and foaming properties, *Colloids Surf., A*, 2001, **189**(1–3), 65–73, DOI: 10.1016/S0927-7757(01)00602-1.

43 H. Wang, X. Wei, Y. Du and D. Wang, Experimental investigation on the dilatational interfacial rheology of dust-suppressing foam and its effect on foam performance, *Process Saf. Environ. Prot.*, 2019, **123**, 351–357, DOI: 10.1016/j.psep.2019.01.027.

This journal is © The Royal Society of Chemistry 2024

Published on 23 October 2024. Downloaded on 11/23/2024 3:26:02 AM.

44 N. Brown, A. de la Pena and S. Razavi, Interfacial rheology insights: particle texture and Pickering foam stability, *J. Phys.: Condens. Matter*, 2023, **35**(38), 4002–4016, DOI: **10.1088/1361-648x/acde2c**.

45 A. C. Martinez, E. Rio, G. Delon, A. Saint-Jalmes, D. Langevin and B. P. Binks, On the origin of the remarkable stability of aqueous foams stabilised by nanoparticles: Link with microscopic surface properties, *Soft Matter*, 2008, **4**(7), 1531–1535, DOI: **10.1039/b804177f**.

46 A. Stocco, W. Drenckhan, E. Rio, D. Langevin and B. P. Binks, Particle-stabilised foams: an interfacial study, *Soft Matter*, 2009, **5**(11), 2215–2222, DOI: **10.1039/b901180c**.

47 D. Georgieva, A. Cagna and D. Langevin, Link between surface elasticity and foam stability, *Soft Matter*, 2009, **5**(10), 2063–2071, DOI: **10.1039/b822568k**.

48 S. Hilgenfeldt, S. A. Koehler and H. A. Stone, Dynamics of coarsening foams: Accelerated and self-limiting drainage, *Phys. Rev. Lett.*, 2001, **86**(20), 4704, DOI: **10.1103/PhysRevLett.86.4704**.

49 A. Saint-Jalmes, Physical chemistry in foam drainage and coarsening, *Soft Matter*, 2006, **2**(10), 836–849, DOI: **10.1039/b606780h**.

50 T. Tamura, Y. Kaneko and M. Ohyama, Dynamic Surface Tension and Foaming Properties of Aqueous Polyoxyethylene n-Dodecyl Ether Solutions, *J. Colloid Interface Sci.*, 1995, **173**(2), 493–499, DOI: **10.1006/jcis.1995.1351**.

51 P. Kanokkarn, T. Shiina, M. Santikunaporn and S. Chavadej, Equilibrium and dynamic surface tension in relation to diffusivity and foaming properties: Effects of surfactant type and structure, *Colloids Surf., A*, 2017, **524**, 135–142, DOI: **10.1016/j.colsurfa.2017.04.043**.

52 R. Bois, O. Adriao, G. Delaplace, I. Pezron, A. Nesterenko and E. Van-Hecke, Influence of process variables on foaming ability of surfactants: Experimental study and dimensional analysis, *Chem. Eng. Res. Des.*, 2021, **165**, 40–50, DOI: **10.1016/j.cherd.2020.10.021**.

53 G. Mary, S. Mezdour, G. Delaplace, R. Lauhon, G. Cuvelier and F. Ducept, Modelling of the continuous foaming operation by dimensional analysis, *Chem. Eng. Res. Des.*, 2013, **91**(12), 2579–2586, DOI: **10.1016/j.cherd.2013.05.020**.

54 M. Zhou and R. Foudazi, Effect of Cosurfactant on Structure and Properties of Polymerized High Internal Phase Emulsions (PolyHIPEs), *Langmuir*, 2021, **37**(26), 7907–7918, DOI: **10.1021/acs.langmuir.1c00419**.

55 M. Zhou, A. Bandegi and R. Foudazi, Control of pore interconnectivity in emulsion-templated porous polymers, *Polymer*, 2023, **281**, 126085, DOI: **10.1016/j.polymer.2023.126085**.

56 C. Kotsmar, J. Krägel, V. I. Kovalchuk, E. V. Aksenenko, V. B. Fainerman and R. Miller, Dilation and shear rheology of mixed β-casein/surfactant adsorption layers, *J. Phys. Chem. B*, 2009, **113**(1), 103–113, DOI: **10.1021/jp807197s**.

57 F. Ravera, G. Loglio and V. I. Kovalchuk, Interfacial dilational rheology by oscillating bubble/drop methods, *Curr. Opin. Colloid Interface Sci.*, 2010, **15**(4), 217–228, DOI: **10.1016/j.cocis.2010.04.001**.

58 P. Amani and M. Firouzi, Effect of salt and particles on the hydrodynamics of foam flows in relation to foam static characteristics, *Chem. Eng. Sci.*, 2022, **254**, 117611, DOI: **10.1016/j.ces.2022.117611**.

59 P. Amani, S. I. Karakashev and N. A. Grozev, *et al.*, Effect of selected monovalent salts on surfactant stabilized foams, *Adv. Colloid Interface Sci.*, 2021, **295**, 102490, DOI: **10.1016/j.cis.2021.102490**.

60 K. Feitosa, S. Marze, A. Saint-Jalmes and D. J. Durian, Electrical conductivity of dispersions: From dry foams to dilute suspensions, *J. Phys.: Condens. Matter*, 2005, **17**(41), 6301–6305, DOI: **10.1088/0953-8984/17/41/001**.

61 N. Yekeen, M. A. Manan, A. K. Idris and A. M. Samin, Influence of surfactant and electrolyte concentrations on surfactant Adsorption and foaming characteristics, *J. Pet. Sci. Eng.*, 2017, **149**, 612–622, DOI: **10.1016/j.petrol.2016.11.018**.

62 M. R. Behera, S. R. Varade, P. Ghosh, P. Paul and A. S. Negi, Foaming in micellar solutions: Effects of surfactant, salt, and oil concentrations, *Ind. Eng. Chem. Res.*, 2014, **53**(48), 18497–18507, DOI: **10.1021/ie503591v**.

63 A. Nguyen and H. J. Schulze, *Colloidal Science of Flotation*, CRC Press, 2003, DOI: **10.1201/9781482276411**.

64 W. Drenckhan and A. Saint-Jalmes, The science of foaming, *Adv. Colloid Interface Sci.*, 2015, **222**, 228–259, DOI: **10.1016/j.cis.2015.04.001**.

65 J. Yang, K. Yu, T. Tsuji, R. Jha and Y. Y. Zuo, Determining the surface dilational rheology of surfactant and protein films with a droplet waveform generator, *J. Colloid Interface Sci.*, 2019, **537**, 547–553, DOI: **10.1016/j.jcis.2018.11.054**.

66 A. Martínez-Calvo and A. Sevilla, Universal Thinning of Liquid Filaments under Dominant Surface Forces, *Phys. Rev. Lett.*, 2020, **125**(11), 114502, DOI: **10.1103/PHYSREVLETT.125.114502**.

67 A. V. Nguyen, Liquid drainage in single Plateau borders of foam, *J. Colloid Interface Sci.*, 2002, **249**(1), 194–199, DOI: **10.1006/jcis.2001.8176**.

68 P. Stevenson, Dimensional analysis of foam drainage, *Chem. Eng. Sci.*, 2006, **61**(14), 4503–4510, DOI: **10.1016/j.ces.2006.02.026**.

69 F. Rouyer, B. Haffner, N. Louvet, Y. Khidas and O. Pitois, Foam clogging, *Soft Matter*, 2014, **10**(36), 6990–6998, DOI: **10.1039/c4sm00496e**.

70 A. Maestro, E. Rio, W. Drenckhan, D. Langevin and A. Salonen, Foams stabilised by mixtures of nanoparticles and oppositely charged surfactants: Relationship between bubble shrinkage and foam coarsening, *Soft Matter*, 2014, **10**(36), 6975–6983, DOI: **10.1039/c4sm00047a**.

71 S. Barman, M. L. Davidson, L. M. Walker, S. L. Anna and J. A. Zasadzinski, Inflammation product effects on dilatational mechanics can trigger the Laplace instability and acute respiratory distress syndrome, *Soft Matter*, 2020, **16**(29), 6890–6901, DOI: **10.1039/d0sm00415d**.

72 A. K. Ndiritu, J. N. Kinyuru, P. N. Gichuhi and G. M. Kenji, Effects of NaCl and pH on the functional properties of edible crickets (Acheta domesticus) protein concentrate, *J. Food Meas. Charact.*, 2019, **13**, 1788–1796, DOI: **10.1007/s11694-019-00097-5**.

73 O. S. Lawal, Functionality of African locust bean (Parkia biglobossa) protein isolate: Effects of pH, ionic strength and various protein concentrations, *Food Chem.*, 2004, **86**(3), 345–355, DOI: **10.1016/j.foodchem.2003.09.036**.